npj | climate and atmospheric science

Article

Published in partnership with CECCR at King Abdulaziz University

https://doi.org/10.1038/s41612-025-01105-w

Strengthened influence of Atlantic Niño on ENSO in a warming climate

Lei Zhang[1,2,3] ✉, Chunzai Wang[1,2,3] ✉, Weiqing Han[4], Kristopher B. Karnauskas[4,5], Michael J. McPhaden[6], Aixue Hu[7], Wen Xing[1,2], Baiyang Chen[1,2] & Heng Liu[1,2,8]

Atlantic Niño can influence ENSO by modulating the Pacific Walker circulation. This interbasin connection is dominated by central Atlantic Niño (CAN) events, which began to emerge around 2000. Our analysis of observational data and climate model simulations reveals that the influence of CAN on ENSO will strengthen in a warming climate due to an enhanced Pacific response. On one hand, increased variability of the eastern Pacific intertropical convergence zone leads to stronger subsidence anomalies induced by CAN; on the other hand, strengthened atmospheric variability over the North Indian Ocean enhances the region's response to CAN-induced Kelvin waves, promoting easterly anomalies over the western tropical Pacific. These changes are further linked to the pronounced interhemispheric warming contrast projected by climate models. Our findings underscore the growing influence of Atlantic Niño on ENSO, with important implications for seasonal climate prediction and future climate change projections.

El Niño–Southern Oscillation (ENSO) refers to the year-to-year fluctuations in the tropical Pacific coupled climate system, characterized by substantial changes in sea surface temperature (SST), winds, and rainfall across the central and eastern tropical Pacific Ocean[1,2]. Through atmospheric teleconnections, ENSO exerts significant influences on global weather and climate conditions including extreme events[3,4]. Hence, an accurate forecast of ENSO is of paramount importance for effective societal preparedness against abnormal climate patterns, thereby mitigating potential economic losses and yielding substantial societal benefits[5–7]. However, the present state of ENSO prediction is still not satisfactory, which is partly due to our incomplete understanding of its underlying physical drivers[8,9].

ENSO primarily arises from coupled interactions between the atmosphere and ocean in the tropical Pacific, known as the Bjerknes feedback[10]. Furthermore, it has been widely acknowledged that external influences from other tropical ocean basins can also impact the development and decaying phases of ENSO[11–22]. For example, Atlantic Niño, the primary mode of interannual climate variability in the tropical Atlantic Ocean, reaching its peak during boreal summer[23–25], is capable of generating cold SST anomalies (SSTAs) in the tropical Pacific. This occurs through the strengthening of the descending motion over the eastern tropical Pacific, driven by the ascending motion anomalies over the tropical Atlantic; consequently, the Pacific Walker circulation strengthens during Atlantic Niño, subsequently leading to the development of La Niña in the following winter[16,17,26–32]. Additionally, the influence of Atlantic Niño on La Niña can also occur through driving easterly wind anomalies over the tropical Indian Ocean and the western tropical Pacific as atmospheric Kelvin waves[33,34]. Notably, Atlantic Niño may have also played a role in contributing to the recent so-called "triple-dip" La Niña during 2020–2022[35,36]. Similarly, Atlantic Niña can induce El Niño conditions in the Pacific. Hence, Atlantic Niño/Niña serves as a significant precursor for ENSO, enhancing its prediction skill[37–43]. However, the physical linkage between Atlantic Niño and ENSO remains a subject of vigorous debate[44–46].

Furthermore, as the global mean surface temperature rises due to increased emissions of anthropogenic greenhouse gases, substantial changes in the mean state and variability of tropical basins have occurred in recent decades[47–59]. These changes may alter the remote influence of Atlantic Niño on ENSO. For instance, it has been suggested that the triggering effect of the summertime Atlantic Niño on the subsequent development of La Niña is projected to weaken in the future under global warming[60]. This weakening is attributed to enhanced tropospheric stability, which weakens the Atlantic rainfall anomalies associated with Atlantic Niño and thereby diminishes the Pacific response[60–62]. On the other hand, it has been suggested that the

[1]State Key Laboratory of Tropical Oceanography, South China Sea Institute of Oceanology, Chinese Academy of Sciences, Guangdong, Guangzhou, China. [2]Global Ocean and Climate Research Center, South China Sea Institute of Oceanology, Chinese Academy of Sciences, Guangdong, Guangzhou, China. [3]Guangdong Key Laboratory of Ocean Remote Sensing, South China Sea Institute of Oceanology, Chinese Academy of Sciences, Guangzhou, China. [4]Department of Atmospheric and Oceanic Sciences, University of Colorado, Boulder, CO, USA. [5]Cooperative Institute for Research in Environmental Sciences, University of Colorado, Boulder, CO, USA. [6]National Oceanic and Atmospheric Administration/Pacific Marine Environmental Laboratory, Seattle, WA, USA. [7]National Center for Atmospheric Research, Boulder, CO, USA. [8]University of Chinese Academy of Sciences, Beijing, China. ✉e-mail: zhanglei@scsio.ac.cn; cwang@scsio.ac.cn

Atlantic warming in recent decades could enhance the impact of Atlantic Niño on ENSO[63]. These results indicate that changes in the Atlantic Niño–ENSO connection in a warming climate remains somewhat uncertain.

Analogous to the paradigm shift in ENSO research over the past two decades[64], two distinct types of Atlantic Niño have been identified recently–the central (CAN) and eastern Atlantic Niño (EAN)–motivated by changes in the dominant pattern of Atlantic Niño in recent decades[65]. CAN is located at the edge of the Atlantic warm pool with a large SST warming in the central basin (Fig. 1b), while the eastern type primarily exhibits warming anomalies in the cold tongue region (Fig. 1a). Consequently, CAN can induce more pronounced wind and rainfall changes over the tropical Atlantic Ocean due to higher background SST, thereby exerting more significant remote impacts on ENSO (Fig. 1d)[66–68] and the European climate[69] through atmospheric teleconnections. Meanwhile, observations suggest a substantial weakening of EAN since the 1970s likely owing to the deepening of the thermocline in the eastern tropical Atlantic[65], in contrast to the relatively stable strength of CAN during the same period (Fig. 1c). As a result, CAN has emerged as the predominant flavor of Atlantic Niño governing the remote influence on ENSO since 2000. These changes are partly linked to interdecadal shifts in the prevailing patterns and climate impacts of the Atlantic Niño, as previously reported[70–75]. The distinct climatic impacts between the two Atlantic Niño types are consistently represented in state-of-the-art global climate models, which depict a stronger remote impact of CAN compared to EAN (Fig. 1e).

Given the distinct remote influences of CAN and EAN on ENSO, as observed in both observational data and climate models, it becomes imperative to investigate how their effects on ENSO might evolve in the future under ongoing emissions of anthropogenic greenhouse gases. This connection holds considerable significance for projecting future climate change and also acts as a source of seasonal-to-interannual climate predictability. Here, through analysis of observational data sets and simulations from the Couple Model Intercomparison Project Phase 6 (CMIP6) (Supplementary Table S1), we characterize and explain the changes in the Atlantic Niño–ENSO connection under global warming. Due to the emerging dominance of CAN in the Atlantic–Pacific interaction, our study unravels changes in its impact in a warming climate.

Results

Atlantic Niño in CMIP6 models

To investigate the influences of CAN and EAN on ENSO in CMIP6 models, we first distinguish and characterize these two types in the models. Most previous studies utilize the ATL3 index[16,17,76], defined as SSTAs averaged over the central–eastern equatorial Atlantic Ocean, to represent Atlantic Niño (see Methods). However, both CAN and EAN are associated with significant warming in the ATL3 region, and consequently, the index is inadequate for distinguishing between the two Atlantic Niño types and their respective climatic impacts[65]. To overcome this limitation, we employ Empirical Orthogonal Function (EOF) analysis of tropical Atlantic SSTAs (see Methods), following ref. 65. The leading mode (EOF1) describes the overall Atlantic Niño pattern with warming in both the central and eastern tropical Atlantic Ocean. The third EOF mode (EOF3) exhibits a zonal contrast pattern with opposite SST changes between the western and eastern basins, delineating the east-west shift of the warming center (Supplementary Fig. S1). As the Atlantic Niño warming center has primarily exhibited an east-west migration in recent decades, EOF3 effectively characterizes its pattern diversity[65]. Hence, by combining these two EOF modes and their corresponding principal components (PCs), we distinguish the two types of Atlantic Niño and obtain their respective indices–the CANI and EANI (see Methods).

We next compare the two Atlantic Niño types between observations and CMIP6 simulations during the historical period to assess the models' ability to capture them (Supplementary Fig. S1). It is noted that climate models tend to underestimate the eastern Atlantic coastal warming associated with Atlantic Niño, possibly stemming from deficiencies in simulating the coastal dynamic processes and interbasin impact from the tropical Indian Ocean[77] or being linked to mean state SST biases in the eastern basin[78,79]. This bias may lead to an underestimation of EAN and its associated impacts. Despite this limitation, CMIP6 models appear to effectively distinguish between CAN and EAN. Moreover, most CMIP6 models consistently illustrate a more robust CAN–ENSO than EAN–ENSO connection (Fig. 1e), similar to the stronger connection between CAN and ENSO compared to the EAN in observations since 2000 (Fig. 1d). On the other hand, the ATL3–ENSO correlation falls between those for the two Atlantic Niño types in CMIP6 models, whereas observations show a generally higher correlation between ENSO and ATL3 than with CAN (Supplementary Fig. S2). This discrepancy may reflect the influence of natural variability in the observations. Overall, these results underscore the dominance of CAN in describing the remote influence of Atlantic Niño on ENSO.

On the other hand, it is noted that CMIP6 model results exhibit a considerable spread in Atlantic Niño–ENSO connections (Fig. 1e). For instance, some models simulate overly weak CAN–ENSO correlations, or even show opposite (positive) ATL3–ENSO and EAN–ENSO correlations. To explore future changes in the Atlantic Niño's impact on ENSO, we select a subset of CMIP6 models that can faithfully simulate the observed relationship between the two during the historical period. We first evaluate the ability of models to capture the overall Atlantic Niño pattern (Fig. 2a), and then rank them based on the simulated Atlantic Niño–ENSO connections (Fig. 2b). Given the dominant influence of CAN on ENSO, we use the CAN–ENSO correlation as the criterion, selecting 22 models that offer the most accurate representation of the CAN's influence on ENSO for our analysis (see Methods). These chosen models indeed show a more pronounced ENSO response compared to those excluded from the selection (Fig. 2c–h).

Strengthened Atlantic Niño–ENSO connection

Using the selected CMIP6 models, we examine future changes in the Atlantic Niño's influence on the subsequent development of ENSO under global warming. We compare the correlation between Atlantic Niño in boreal summer and ENSO in the following winter for the historical period (1970–2022) and future projections (2050–2100). Results show that approximately 70% (15 of 22) of the models simulate a more robust CAN–ENSO connection under global warming (Fig. 3a). Additionally, multi-member mean results also suggest a ~11% strengthening in the CAN–ENSO correlation in a warming climate, which is statistically significant at the 90% confidence level based on a bootstrap test (see Methods). The ensemble mean increase appears modest due to cancellations across different models, suggesting some uncertainties in the projected changes in the CAN–ENSO connection. Nevertheless, these results suggest a strengthened influence of CAN on ENSO in a warming climate. In contrast, the EAN–ENSO correlation weakens in the majority of models (Fig. 3c), with insignificant multi-member mean changes. Due to these differences between CAN and EAN, the future change in the ATL3–ENSO correlation remains somewhat uncertain (Supplementary Fig. S3a). Nevertheless, considering the predominant influence of CAN on ENSO in both observations and CMIP6 historical simulations, these results indicate a strengthened impact of Atlantic Niño on ENSO in a warming climate.

The remote influence of Atlantic Niño on ENSO occurs through two main pathways. First, it strengthens the subsidence branch of the Walker circulation in the adjacent Pacific sector[16]. Second, it induces eastward-propagating Kelvin waves, leading to easterly wind anomalies over the tropical Indian Ocean and western tropical Pacific[33,34]. Indeed, the selected models show that CAN induces substantial upward motion anomalies over the tropical Atlantic Ocean, which enhance subsidence over the eastern tropical Pacific and induce ascending anomalies over the tropical Indian Ocean-western tropical Pacific that promote easterly wind anomalies in the region. Together, these changes enhance low-level easterly winds across the tropical Pacific, resulting in cold SSTAs in the region (Figs. 2c–e and 4a, b). Conversely, owing to its location and cooler background SSTs, the

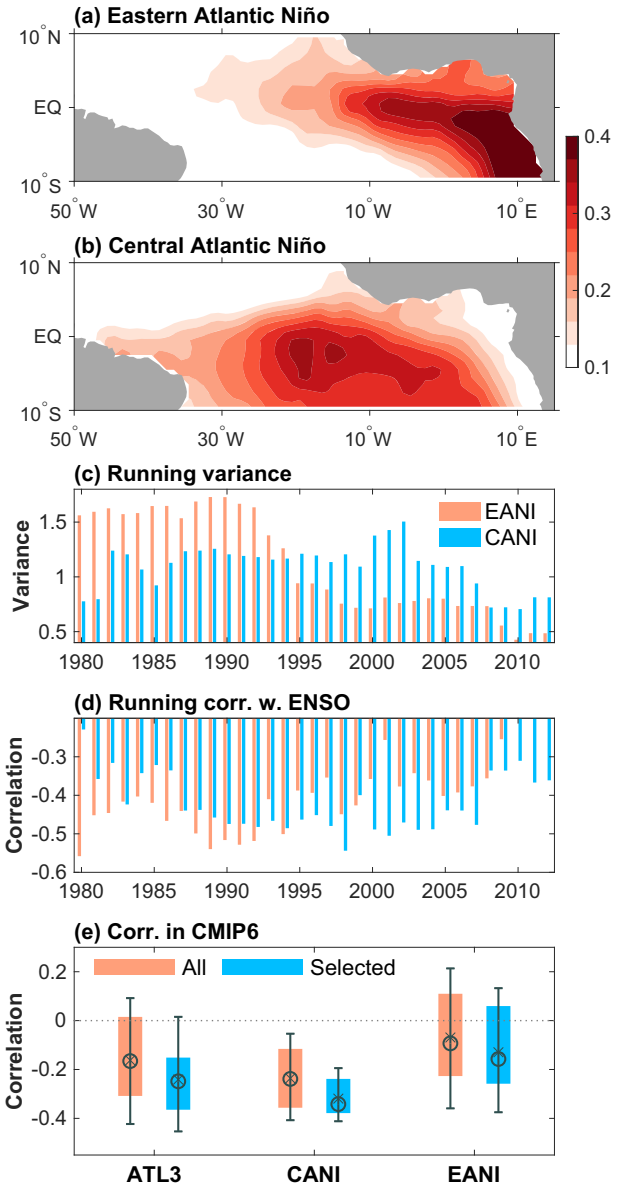

Fig. 1 | Two types of Atlantic Niño. a, **b** The eastern (EAN) and central Atlantic Niño (CAN), obtained through combinations of the first and third modes of the empirical orthogonal function (EOF) analysis using HadISST during 1970–2022 (Supplementary Fig. S1) (see Methods). **c** 21-year running variance of the normalized June-July-August (JJA)-mean EANI (orange) and CANI (blue). **d** 21-year running correlation between the two indices during JJA and the Niño-3.4 index during December-January-February (DJF). **e** Correlations between Atlantic Niño indices during JJA and the Niño-3.4 index during DJF for the period 1970–2022. The first column denotes the ATL3–ENSO correlation, the second column for the CANI–ENSO correlation and the third column for the EANI–ENSO correlation. Orange represents all models from Coupled Model Intercomparison Phase 6 (CMIP6) analyzed in this study, and blue represents results from the selected CMIP6 models (Fig. 2; see Methods). Circles and cross signs represent the median and mean values, respectively. Error bars denote 25th to 75th percentiles, and vertical lines denote 10th to 90th percentiles.

anomalous ascending motion associated with EAN is located exclusively within the eastern tropical Atlantic Ocean, exerting a negligible influence on ENSO (Fig. 4d, e). Notably, compared to the historical period, CAN induces stronger subsidence and easterly wind anomalies over the eastern Pacific, as well as enhanced ascending anomalies over the tropical Indian Ocean in CMIP6 future projections (Fig. 4c and Supplementary Fig. S4b). This result explains the strengthened CAN–ENSO connection under global warming as identified above, while the impact of EAN on ENSO remains weak (Fig. 4e–f).

In contrast to the enhanced Pacific response, the ascending anomalies and positive rainfall changes over the tropical Atlantic induced by CAN are projected to weaken in the future compared to the historical period (Fig. 4c and Supplementary Fig. S4a). This is likely attributable to changes in the strength of CAN itself. Previous studies have suggested a weakening trend of Atlantic Niño over recent decades, and projections suggest a further decline in the strength of Atlantic Niño due to the deepening of the thermocline in the tropical Atlantic in a warming climate[55,56,58]. Indeed, the majority of the selected CMIP6 models project weaker ATL3 variance in the future (Supplementary Fig. S3b). Further analysis reveals that the weakening of Atlantic Niño is associated with the reduced strength of both CAN and EAN under global warming, with a higher inter-model agreement for the weakening of CAN compared to EAN (Fig. 3b, d). The reduction of the tropical Atlantic SSTA variance in CMIP6 future projections is also primarily observed in the central equatorial region (Supplementary Fig. S5b). These results suggest that CAN is associated with weaker SSTAs in future projections. Due to the nonlinear dependence of tropical rainfall on SST[66,67], the atmospheric response to CAN becomes less pronounced under global warming (Supplementary Fig. S6). Additionally, the increased tropospheric stability in a warming climate may also contribute to the suppression of the Atlantic rainfall response to the warm SSTAs during Atlantic Niño[60].

The enhanced Pacific response

The findings above suggest that the strengthened CAN–ENSO connection in CMIP6 future projections primarily arises from the enhanced Pacific response to the CAN forcing, despite the concurrent weakening of the tropical Atlantic rainfall anomalies induced by CAN (Supplementary Fig. S6). Next, we explore changes in the two main pathways through which Atlantic Niño influences ENSO: Strengthening of the subsidence branch of the Pacific Walker circulation in the eastern tropical Pacific[16] and the eastward-propagating Kelvin waves that influence the tropical Indian Ocean and western tropical Pacific[33,34].

In the eastern tropical Pacific–the key region for the westward pathway–changes in winds and rainfall are closely linked to the variability of the Intertropical Convergence Zone (ITCZ)[80]. Indeed, the CAN-induced dry anomalies, enhanced subsidence, and low-level divergence anomalies over the eastern tropical Pacific are mainly located in the ITCZ region (Supplementary Fig. S6a, b). Notably, the stronger CAN-induced descending motion and negative rainfall anomalies in the eastern Pacific under global warming are also primarily found over the ITCZ region (Supplementary Fig. S6c). A linear baroclinic model[81] experiment shows that dry anomalies over the Pacific ITCZ can induce prominent easterly wind anomalies over the tropical Pacific (Supplementary Fig. S7; see Methods). These results suggest that the amplified Pacific changes driven by CAN in a warming climate are closely associated with changes in the Pacific ITCZ.

Atlantic Niño can also induce eastward-propagating atmospheric Kelvin waves that influence ENSO by generating easterly wind anomalies over the tropical Indian Ocean. The wind anomalies counteract the prevailing westerly monsoon circulation during boreal summer, leading to warm SSTAs north of the equator through the "wind-evaporation-SST" (WES) mechanism, and enhancing local rainfall (Supplementary Figs. S8 and S9). Subsequently, the anomalous heating over the tropical Indian Ocean further strengthens easterly wind anomalies over the western tropical Pacific, promoting the development of cold SSTAs in the basin. This pathway is also projected to strengthen in a warming climate (Supplementary Figs. S8c and S9c), contributing to the enhanced Pacific response to CAN forcing.

The two pathways are closely linked to atmospheric variability in the Pacific ITCZ and the North Indian Ocean, respectively. In CMIP6 future projections, the variance of the rainfall and vertical motion anomalies in both regions increases (Fig. 4g–i, and Supplementary Fig. S10). As a result, these areas become more sensitive to CAN-induced circulation changes,

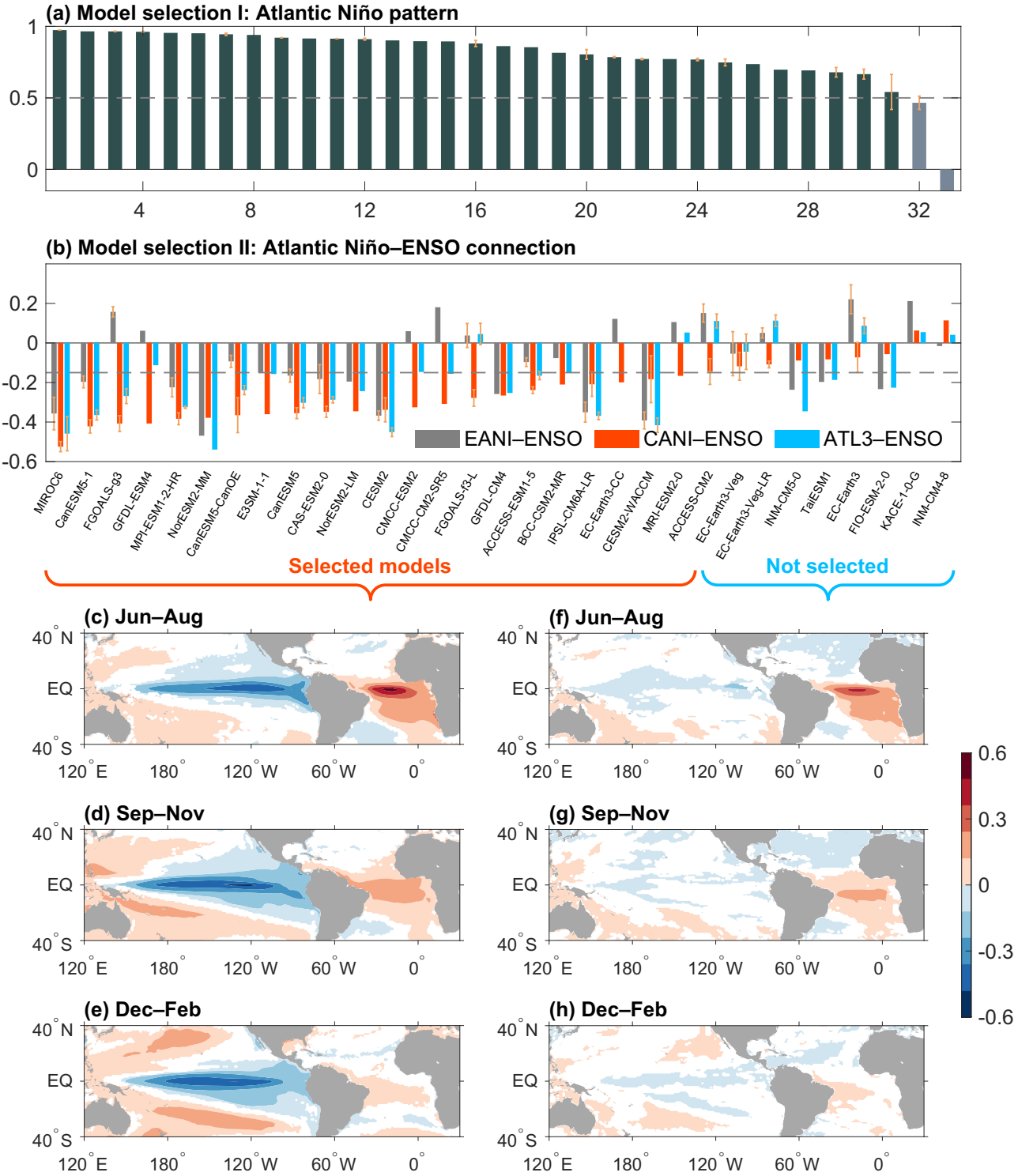

Fig. 2 | Selection of CMIP6 models. a Pattern correlation coefficients between the EOF1 mode in CMIP6 models and observations (see Methods). The horizontal dashed line denotes the selection criterion ($r \geq 0.5$). Dark colors denote the selected models, and light colors denote unselected models. **b** Correlation coefficient between Atlantic Niño indices in JJA and the Niño-3.4 index in DJF for the period 1970–2022. Gray bars denote the correlation for EANI–ENSO, red for CANI–ENSO, and blue for ATL3–ENSO. The horizontal dashed line denotes the selection criterion ($r \leq -0.15$). The models are ranked and selected based on the CANI–ENSO correlation, considering the dominance of CAN in influencing ENSO (Fig. 1e). Error bars in (**a**) and (**b**) represent uncertainties across different model members (with at least 2 members) assessed based on a bootstrapping test (see Methods). **c** Regression of JJA-mean sea surface temperature anomalies (SSTAs) on the normalized JJA-mean CANI for the period 1970–2022 in selected models in (**b**). Unit is °C. **d**, **e** As in (**c**), except for regressions of the September–November (SON)-mean and DJF-mean SSTAs. **f**–**h** As in (**c**)–(**e**), except for the unselected models. Shading in (**c**)–(**h**) denote the regions where more than 70% of the models agree with signs of the regression results.

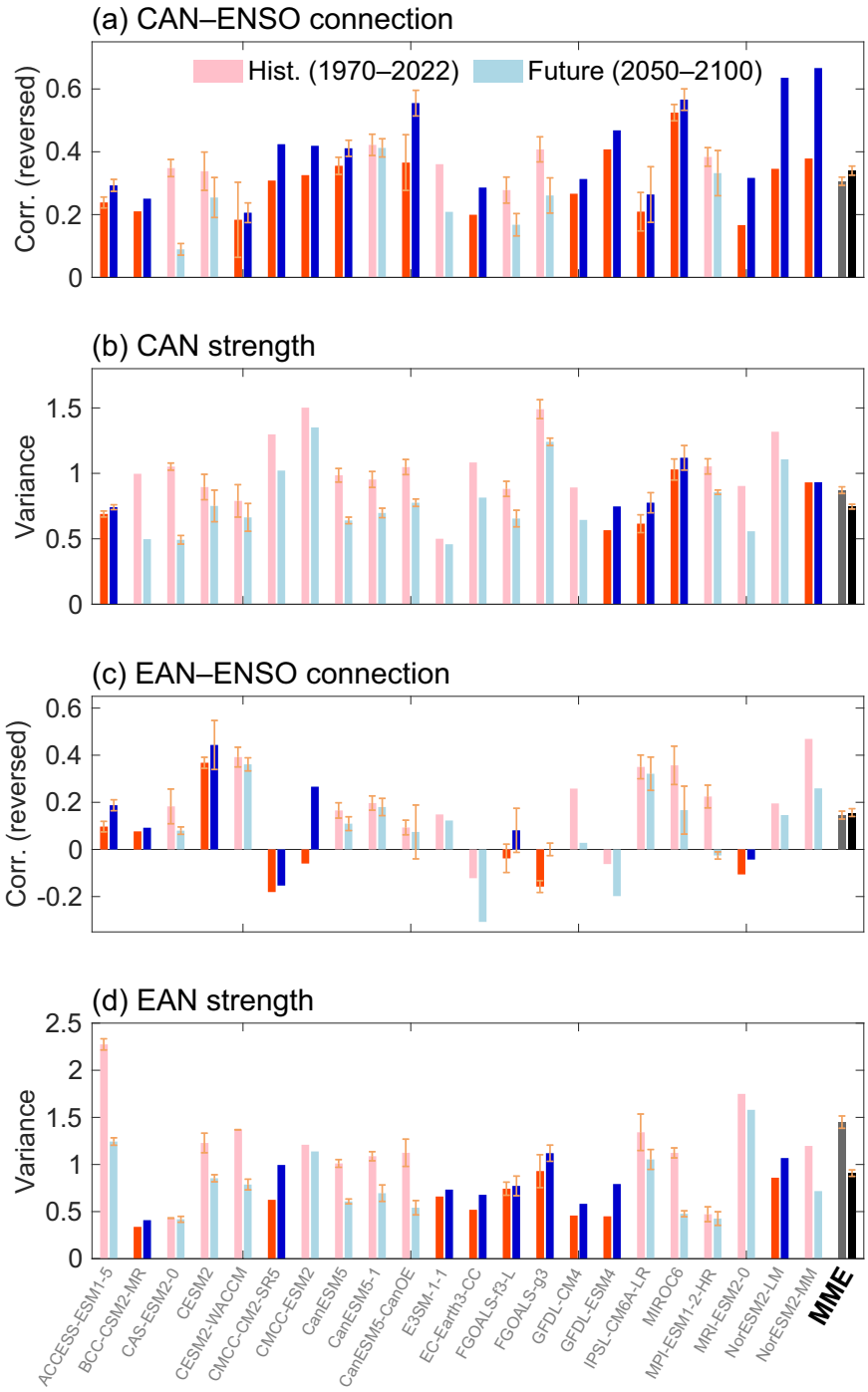

Fig. 3 | Changes in the Atlantic Niño–ENSO connection. a The CANI–ENSO correlation during the historical period (red) and future projections (blue) in the selected CMIP6 models (Fig. 2). The correlation coefficient is between JJA-mean CANI and DJF-mean Niño-3.4 index, with the sign reversed. 15 out of 22 models simulate stronger CANI–ENSO correlations in future projections compared to historical period, which are shown in dark colors. Error bars represent uncertainties across different model members (with at least 2 members) obtained through a bootstrapping test (see Methods). Multi-member mean (MME) results during historical period (gray) and future projections (black) are shown in the last column, with mean values and error bars assessed based on 115 members of 22 selected models. **b** As in (**a**), but for the CANI variance. **c**, **d** As in (**a**, **b**), except for the EANI results.

leading to stronger responses to the CAN forcing. Thus, the intensified Pacific response to CAN can be primarily attributed to the increased atmospheric variability of the Pacific ITCZ and North Indian Ocean under global warming.

Variability in the ITCZ[80,82] and Indian summer monsoon[83,84] has both been linked to the interhemispheric thermal contrast. In CMIP6 future projections, a salient feature is the faster warming rate of the Northern Hemisphere compared to the Southern Hemisphere (Fig. 5a). This warming contrast increases the interhemispheric temperature gradient during boreal summer, enhancing moisture and energy supply to the Northern Hemisphere, thus creating more favorable conditions for establishment of convections. Consequently, atmospheric variability in the eastern Pacific ITCZ and North Indian Ocean–two major rainfall centers in the Northern Hemisphere and key regions for the Atlantic Niño's influence on ENSO–strengthens (Supplementary Fig. S10b, d).

The magnitude of the interhemispheric warming contrast across CMIP6 models is indeed associated with changes in the rainfall variability of the Pacific ITCZ and North Indian Ocean, with correlations exceeding the 90% confidence level (Supplementary Fig. S11a, b). Moreover, the interhemispheric thermal contrast has a more pronounced impact on the dynamic (wind) component of the ITCZ and Indian summer monsoon compared to the thermodynamic (rainfall) component. These findings suggest that the enhanced interhemispheric thermal contrast amplifies the variability of the ITCZ and the Indian summer monsoon, making these regions more susceptible to CAN forcing in a warming climate. Additionally, equatorial Pacific SST anomalies may also influence the Pacific ITCZ

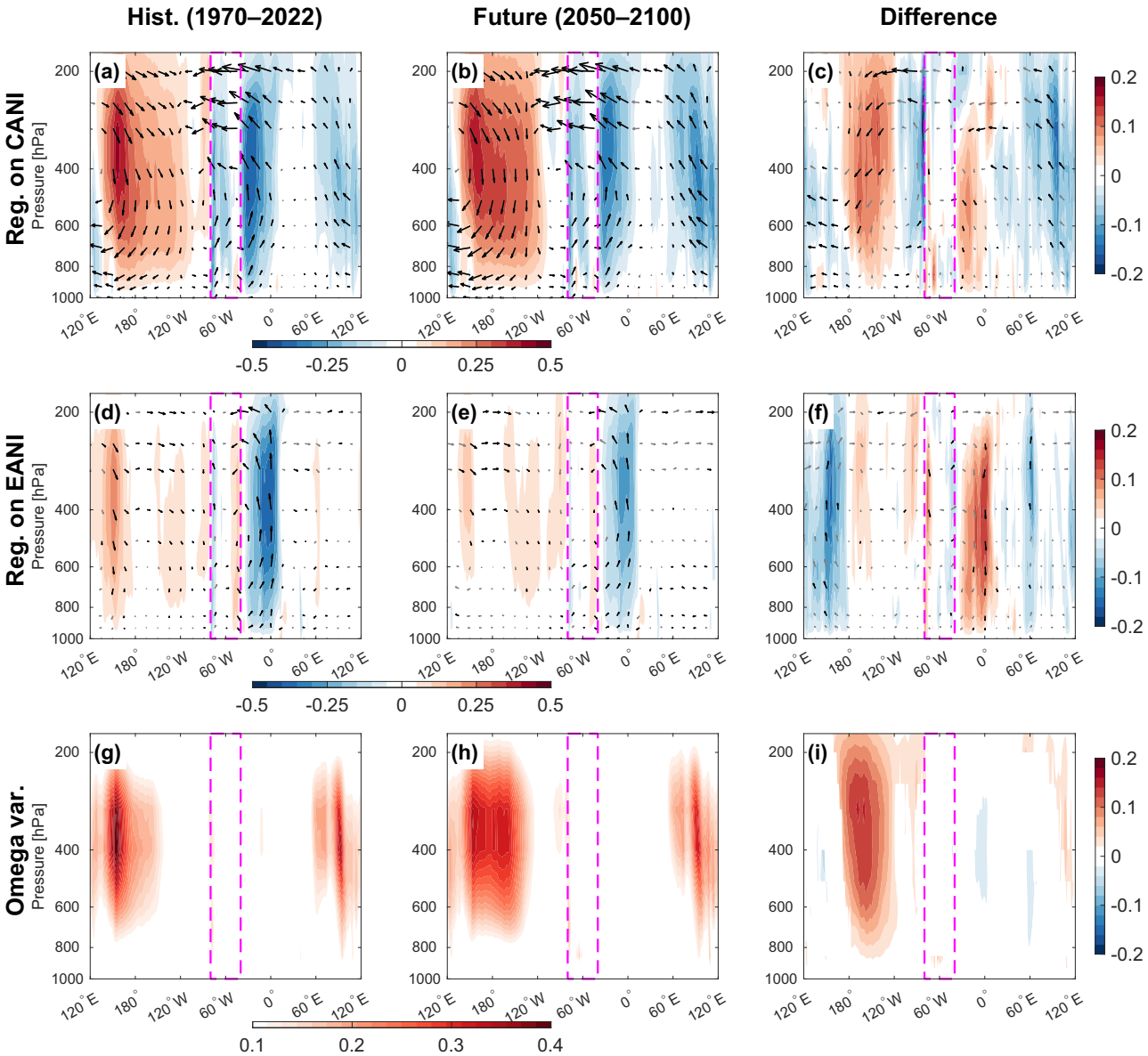

Fig. 4 | Enhanced Pacific response to CAN. a Shading denotes regression of the JJA-mean omega averaged within 15°N–15°S on the normalized JJA-mean CANI during the historical period. Units are Pa s^{-1}. We have scaled the values of omega by a factor of 120. Vectors denote regression of zonal winds (m s^{-1}) and omega. **b** As in (**a**) except for the future projections. **c** Differences between future projections and historical simulations. **d**–**f** As in (**a**)–(**c**), except for EANI results. **g** Variance of JJA-mean omega during the historical period. Units are Pa^2 s^{-2}. The variance has been scaled by a factor of 2000. **h** As in (**g**) except for the future projections. **i** Differences between historical simulations in (**g**) and future projections in (**h**) (future minus historical). Shown are average of the 22 selected models (Fig. 2). Black vectors in (**a**)–(**f**) and shading in (**i**) denote results for which more than 70% of the models agree with signs of changes. The magenta dashed box denotes South America that separates the tropical Pacific and Atlantic Oceans.

and thereby modulate the Pacific response to CAN. However, the relationship between the eastern equatorial Pacific warming and the CAN-ENSO connection is weak and inconsistent across different CMIP6 models (not shown).

To further explore the impact of interhemispheric thermal contrast on the variability of the ITCZ and Indian summer monsoon, we conducted atmospheric model experiments by applying a uniform 1 °C SST warming in the Northern Hemisphere (see Methods). The model results exhibit some notable discrepancies compared to CMIP6 projections (Supplementary Figs. S10 and S12), which are likely due to the neglect of the non-uniform SST warming pattern. Nevertheless, the model results confirm an increase in the variance of rainfall and circulation in both the eastern Pacific ITCZ and the North Indian Ocean in response to Northern Hemispheric SST warming (Supplementary Fig. S12). These findings suggest that even in the absence of changes in local air-sea interaction processes, the enhanced interhemispheric thermal contrast alone can drive stronger variability in the two regions, thereby enhancing the Pacific response to CAN forcing. Indeed, the enhanced interhemispheric thermal contrast–one of the most robust features in CMIP6 future projections–emerges as the primary driver of the strengthened CAN-ENSO connection in a warming climate, with a correlation of 0.68 between the two across CMIP6 models (Fig. 5b).

Discussion

In this study, we investigate the influence of Atlantic Niño on ENSO in a warming climate. Our findings reveal that the central Atlantic Niño (CAN) plays a pivotal role in influencing ENSO in both observations and CMIP6 historical simulations, and this remote impact will be strengthened under global warming, despite some uncertainties across different models. In

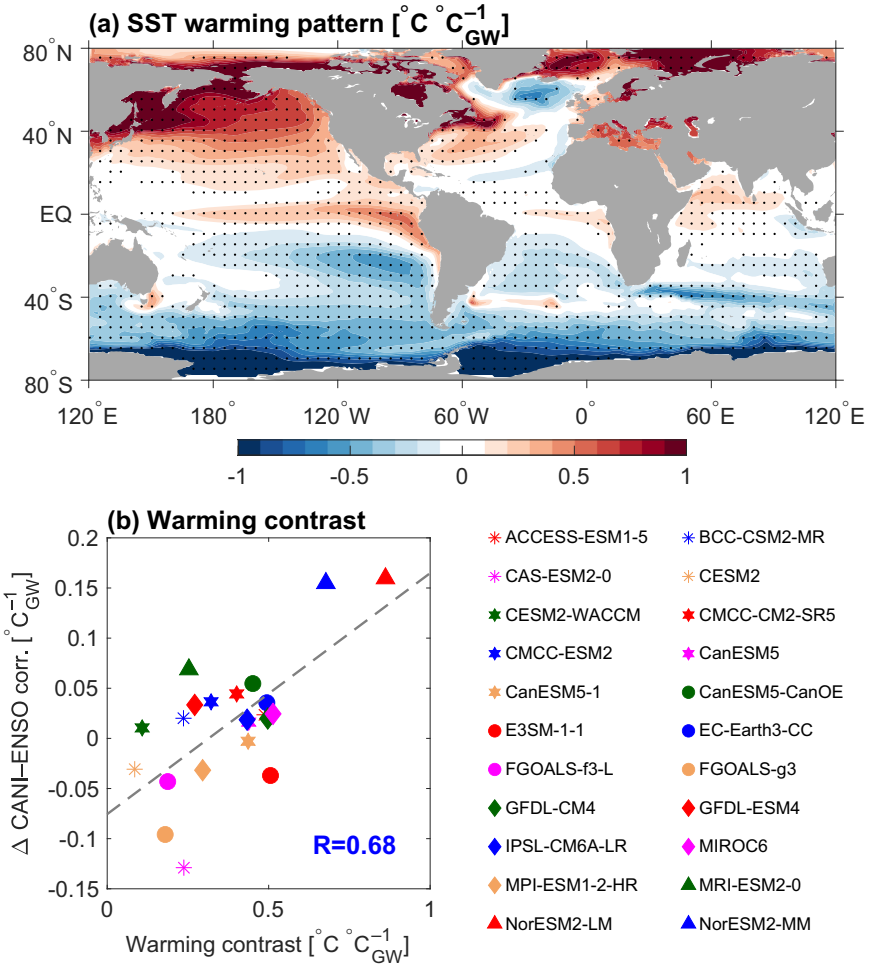

Fig. 5 | The role of interhemispheric warming contrast. a Differences of JJA-mean SSTA (shading; °C °C^{-1}) between the historical period and future projections in the 22 selected CMIP6 models (future minus historical). The global mean SST warming has been removed. Stippling denotes regions where more than 70% of the models agree with signs of SSTAs (with global mean warming removed). **b** Scatter plot of the interhemispheric warming contrast against changes in the CANI–ENSO correlation (sign flipped). The dashed line denotes the linear regression between the two, and their correlation is shown at the lower right corner ($r = 0.68$), which is statistically significant at the 99% confidence level. The interhemispheric warming contrast is defined as differences of SST warming between the Northern (0°–60°N) and Southern Hemisphere (60°S–0°).

contrast, the remote effect of the eastern Atlantic Niño (EAN) on ENSO will remain limited. The more pronounced influence of CAN on ENSO under global warming is primarily associated with the strengthened Pacific response to the CAN-induced rainfall anomalies in the tropical Atlantic Ocean. This change is in turn attributed to the enhanced variance of the Pacific ITCZ and the Indian summer monsoon driven by the prominent warming in the Northern Hemisphere, which increases the sensitivity of the Pacific Walker cell to the CAN forcing.

In our analyses, we note that the two NorESM models simulate notable increases in the CANI–ENSO correlation compared to other models (Fig. 5 and Supplementary Fig. S11). We tested the sensitivity of our results to the removal of the two models (not shown). Even after their removal, there remains a statistically significant association between the interhemispheric warming contrast and the strengthened CANI–ENSO connection ($r = 0.4$, $p < 0.1$). While the influence of the enhanced interhemispheric thermal contrast on changes in rainfall variability over the ITCZ and Indian summer monsoon becomes negligible, its impact on the variability of vertical motion over these regions remain statistically significant at the 90% confidence level. These results suggest that the role of the interhemispheric temperature gradient in modulating the CAN–ENSO connection is robust and not overly dependent on the two NorESM models.

Variations in both the Pacific ITCZ and ENSO have been previously associated with changes in the Atlantic meridional overturning circulation (AMOC)[85–87]. In particular, the AMOC is projected to weaken under global warming[88], which may result in cold SSTAs, higher sea level pressure, and anti-cyclonic wind anomalies over the North Atlantic. The wind anomalies further extend to the eastern tropical Pacific, inducing anomalous northerlies and a southward shift of the ITCZ in the region. Consequently, the annual cycle of the Pacific coupled climate system weakens[89], promoting a stronger ENSO variability[85]. However, the linkage between changes in the North Atlantic mean state and those in the CAN–ENSO connection across the CMIP6 models appears weak (Supplementary Fig. S13). Furthermore, while the ENSO variance indeed increases in the majority of the selected models, its connection to changes in the CAN–ENSO correlation is negligible (Supplementary Fig. S14). Hence, the weakened AMOC does not seem to play an important role in the strengthened influence of CAN on ENSO under global warming.

It has been suggested that the interbasin connection between Atlantic Niño and ENSO may weaken under global warming, owing to increased static stability resulting from greater warming in the upper troposphere[60]. On the other hand, the weak temperature gradient in the free troposphere over the tropical region–a result of the fast wave adjustment[90]–leads to a relatively uniform distribution of upper tropospheric warming. As a result, changes in static stability are largely determined by the inhomogeneous sea surface warming[91]. As the projected Pacific SST warming is generally more pronounced than that in the tropical Atlantic (Fig. 5a), the former region becomes relatively less stable compared to the latter region (Supplementary Fig. S15). Consequently, the Pacific response to the Atlantic Niño forcing is less impacted by the increased stability under global warming. Instead, our analysis suggests that the response of the Pacific sector is strengthened.

It is worth noting that climate models still exhibit notable biases[78], potentially limiting their capacity to accurately simulate tropical climate variability and to predict their future changes. Specifically, observations suggest an evident weakening of EAN in the past few decades, while the strength of CAN has remained relatively stable. In contrast, projections from CMIP6 models show a significant weakening of CAN under global

warming, while changes in the strength of EAN are relatively uncertain. The contrasting results raise questions about whether the observed changes in CAN and EAN are primarily driven by internal climate variability, while the CMIP6 future projections are predominantly linked to anthropogenic greenhouse gas forcing. An alternative possibility is that, due to the persistent bias of CMIP6 models in simulating the eastern Atlantic coastal warming associated with the Atlantic Niño (Supplementary Fig. S1), they underestimate the EAN and fail to capture its weakening, leading to an overall weak variance and impacts of the EAN in the models. Nevertheless, since the influence of EAN on ENSO is weak in both observations and CMIP6 models, this discrepancy likely has a minimal impact on the conclusions of this study.

Given the profound global impacts of ENSO, it is imperative to understand its interactions with neighboring basins to optimize sources of potential predictability at seasonal to interannual time scales. Our findings highlight the pivotal role of CAN in influencing ENSO, emerging as an increasingly significant predictor for ENSO in the future. On the other hand, recent studies have suggested that the association between ENSO and tropical Atlantic climate anomalies may arise from the influence of ENSO on the Atlantic[44,92]. While analysis of observations and CMIP6 models exhibits negligible tropical Pacific signals during boreal winter before the peak of Atlantic Niño in the following summer, both the tropical Atlantic warming and the Pacific cooling occur concurrently in spring (Supplementary Figs. S16 and S17). Therefore, the extent to which ENSO actively connects the two basins remains unclear and warrants further investigation. Nevertheless, our results emphasize the necessity of considering the interbasin connection between CAN and ENSO to enhance seasonal climate prediction and future projections. Moreover, the current generation of climate models still exhibits notable biases in capturing and distinguishing between CAN and EAN, including their remote influences on other regions. Therefore, it is crucial for future studies to explore the underlying causes for these model deficiencies to further improve models' ability to accurately simulate tropical climate variabilities and their interactions.

Methods

Observational data

To characterize the two types of Atlantic Niño and examine their connections with ENSO in observations, we analyzed monthly SST data from the Hadley Centre Sea Ice and SST (HadISST)[93] during 1970–2022. Considering the large uncertainties in SST reconstructions due to the sparsity of observational records[94], we did not analyze the data during earlier periods. We obtain SSTAs by removing monthly climatologies for 1970–2022. We then conducted EOF analysis of the tropical Atlantic SSTAs to obtain the dominant modes of interannual variability in the region (60°W–20°E, 10°S–10°N)[65]. The linear trend was removed from the SSTA field prior to EOF analysis to exclude the anthropogenic global warming trend. The first EOF describes Atlantic Niño as a whole, with prominent warming spanning both the central and eastern tropical Atlantic, while EOF3 exhibits a zonal contrast pattern with opposite signs of SSTA between the western and eastern Atlantic. EOF2 is primarily associated with the Atlantic Meridional Mode[65].

Observations suggest prominent changes in the dominant pattern of Atlantic Niño in recent decades. While Atlantic Niño predominantly exhibited warming in the cold tongue region prior to 2000, the warming center is located in the central basin in recent decades[65]. These results indicate the presence of two distinct types of the Atlantic Niño dominating different periods. Since EOF3 essentially describes the zonal shift of the warming center, we combine EOF1 and EOF3 and use (EOF1 + EOF3)/√2 and (EOF1–EOF3)/√2 to describe the patterns of the EAN and CAN, respectively.

To document the temporal evolution of ENSO, we use the Niño-3.4 index defined as SSTAs averaged over the central tropical Pacific Ocean (170°W–120°W, 5°S–5°N). We also used (PC1 + PC3)/√2 and (PC1–PC3)/√2 as the indices to represent the EAN and CAN, and the ATL3 (20°W–0°, 3°S–3°N) to describe the overall evolution of Atlantic Niño. Previous studies have demonstrated that Atlantic Niño can influence ENSO through atmospheric teleconnection[16,17], and the strength of this interbasin connection was assessed by the correlation coefficient between the Atlantic Niño indices during boreal summer (June–August, JJA) and the Niño-3.4 index during boreal winter (December–February). The statistical significance of the correlation was assessed using the two-sided Student's *t* test. We also obtained signals associated with Atlantic Niño by performing linear regressions of various variables on each of the normalized indices.

CMIP6 models

To explore future changes in the Atlantic Niño–ENSO connection under the influence of anthropogenic global warming, we examined 149 members from 33 coupled climate models that participate in CMIP6 (Supplementary Table S1). We analyzed historical simulations during 1970–2014, and future projections (2015–2100) under Shared Socio-economic Pathway 5-based Representative Concentration Pathway 8.5 forcing scenario (SSP585)[95]. We chose SSP585 as it represents the most severe warming scenarios in CMIP6 models, potentially enhancing the signal-to-noise ratio and thereby facilitating the detection of changes in the Atlantic Niño–ENSO connection in a warming climate. We used monthly SST, surface wind stress, zonal and meridional winds, and precipitation from each member. All the model outputs were linearly interpolated onto a common 1° × 1° grid. Anomaly fields are obtained by removing monthly climatologies during 1970–2100. Some of the CMIP6 models have multiple ensemble members (Supplementary Table S1), which were averaged for each model prior to calculating the multi-model mean results.

To characterize the two types of Atlantic Niño for both the historical period and future projections, we employed a similar EOF analysis on tropical Atlantic SSTAs as described above for observations. Note that not all the CMIP6 models exhibit the zonal contrast pattern in the EOF3 mode; some models depict the observed EOF3 pattern in their EOF4 mode. Additionally, the ACCESS-CM2 model describes Atlantic Niño in the EOF2 mode, instead of EOF1. For these models, we used EOF modes corresponding to the observed EOF1 and EOF3 to obtain CAN and EAN. The period for the EOF analysis was 1970–2100. We did not remove the linear trend in the model results, as it would introduce artificial multi-decadal variability contaminating the EOF results. Instead, we excluded the long-term warming trend by removing linear regression on the time series of global mean SSTA at each grid. The same approach was employed to eliminate the influence of the externally-forced warming trend for other variables.

CMIP6 models exhibit a large spread in simulating the Atlantic Niño pattern and its remote impact on ENSO. Hence, to examine the future changes in the Atlantic Niño–ENSO connection, we selected the models that best replicate the observed interbasin relationship. We first calculated the pattern correlation coefficient of the EOF1 mode between the CMIP6 models and observations, and selected models that can faithfully reproduce the overall Atlantic Niño pattern ($r \geq 0.5$) (Supplementary Figs. S1 and 2a). Among the 33 models (149 members) analyzed, 31 effectively reproduce the observed Atlantic Niño pattern. We next ranked the CMIP6 models based on the simulated Atlantic Niño–ENSO correlation. Note that correlations between different Atlantic Niño indices and ENSO do not vary consistently; models with a high CAN–ENSO correlation may not exhibit strong EAN–ENSO or ATL3–ENSO connections (Fig. 2b). Considering the dominance of CAN in influencing ENSO in both models and observations, we used the CANI–ENSO correlation as the criterion ($r \leq -0.15$) to identify a final subset of CMIP6 models. Out of 31 models, 22 models meet these criteria and are included in our analysis. The criteria were chosen to ensure that the models adequately simulate the Atlantic Niño pattern and its connection with ENSO, while also maintaining a sufficiently large sample size for robust analysis. The results are similar using stricter threshold values (not shown).

To assess the statistical significance of the results from CMIP6 multi-model ensemble, we calculated the sign-agreement across selected models. Changes for which more than 70% of models agree on the sign of anomalies

are considered significant. Additionally, we performed a bootstrapping test to assess the significance of changes in Atlantic Niño variance and its influence on ENSO. Specifically, 10,000 realizations were generated by resampling, with replacement, the values of Atlantic Niño variance or its correlation with ENSO across different CMIP6 models. The standard deviation of the mean values from all realizations was used to estimate the uncertainty range.

Atmospheric model experiments

To investigate the impact of the Pacific SSTAs on the ITCZ, we conducted a suite of atmospheric model experiments using the National Center for Atmospheric Research (NCAR) Community Atmosphere Model 5 (CAM5)[96]. The model resolution was approximately 2.5° × 2°, and each experiment was integrated for 30 years. Given that the model typically takes several years to achieve statistical equilibrium, the initial 5 years were discarded and the subsequent 25 years of outputs were analyzed.

We conducted two experiments to isolate the influence of interhemispheric warming contrast. The control simulation employed monthly SST climatology from the model as the forcing. In the sensitivity experiment, a uniform 1 °C SST warming was applied across the entire Northern Hemisphere oceans, with a sponge layer implemented between the equator and 5°N. The experiments demonstrate that the interhemispheric thermal contrast effectively enhances the atmospheric variability of ITCZ and North Indian Ocean during boreal summer (Supplementary Fig. S12c, f), consistent with CMIP6 simulations. On the other hand, the enhanced ITCZ variance in the model is located slightly north of the target region in this study, likely due to the model bias in simulating areas of high variance in the mean state (Supplementary Fig. S12).

To investigate the impact of Pacific ITCZ changes on ENSO, we conducted idealized experiments using a linear baroclinic model[81] with a resolution of T42L20. In these experiments, we introduced negative heating anomalies in the eastern Pacific ITCZ region (140°W–80°W, 2.5°N–10°N), with a maximum amplitude of –1 K day^{-1} at the center (Supplementary Fig. S7). The heating anomalies peaked in the mid-troposphere, and the mean state was set to boreal summer conditions. The model was integrated for 30 days, and we analyzed the results from the final 20 days.

Data availability

The observational monthly SST data set from HadISST can be downloaded at https://www.metoffice.gov.uk/hadobs/hadisst/data/download.html. The numerical model results in this study are available from the corresponding authors upon request.

Code availability

The scripts used to analyze data is available from the corresponding authors upon request.

Received: 4 February 2025; Accepted: 28 May 2025;
Published online: 10 June 2025

References

1. Philander, S. G. H., Pacanowski, R. C., Lau, N.-C. & Nath, M. J. Simulation of ENSO with a global atmospheric GCM coupled to a high-resolution, tropical Pacific Ocean GCM. *J. Clim.* **5**, 308–329 (1992).
2. McPhaden, M. J., Zebiak, S. E. & Glantz, M. H. ENSO as an integrating concept in earth science. *Science* **314**, 1740–1745 (2006).
3. Wallace, J. M. & Gutzler, D. S. Teleconnections in the geopotential height field during the Northern hemisphere winter. *Mon. Weather Rev.* **109**, 784–812 (1981).
4. Hoskins, B. J. & Karoly, D. J. The steady linear response of a spherical atmosphere to thermal and orographic forcing. *J. Atmos. Sci.* **38**, 1179–1196 (1981).
5. Cane, M. A., Zebiak, S. E. & Dolan, S. C. Experimental forecasts of El Niño. *Nature* **321**, 827–832 (1986).
6. Cane, M. A., Eshel, G. & Buckland, R. W. Forecasting Zimbabwean maize yield using eastern equatorial Pacific sea surface temperature. *Nature* **370**, 204–205 (1994).
7. Ham, Y.-G., Kim, J.-H. & Luo, J.-J. Deep learning for multi-year ENSO forecasts. *Nature* **573**, 568–572 (2019).
8. Lou, J., Newman, M. & Hoell, A. Multi-decadal variation of ENSO forecast skill since the late 1800s. *npj Clim. Atmos. Sci.* **6**, 89 (2023).
9. Zhang, R.-H., Gao, C. & Feng, L. Recent ENSO evolution and its real-time prediction challenges. *Natl. Sci. Rev.* **9**, nwac052 (2022).
10. Bjerknes, J. Atmospheric teleconnections from the equatorial Pacific. *Mon. Weather Rev.* **97**, 163–172 (1969).
11. Izumo, T. et al. Influence of the state of the Indian Ocean Dipole on the following year's El Niño. *Nat. Geosci.* **3**, 168–172 (2010).
12. Luo, J. J. et al. Interaction between El Niño and extreme Indian Ocean dipole. *J. Clim.* **23**, 726–742 (2010).
13. Cai, W. et al. Pantropical climate interactions. *Science* **363**, eaav4236 (2019).
14. Wang, C. Three-ocean interactions and climate variability: a review and perspective. *Clim. Dyn.* **53**, 5119–5136 (2019).
15. Behera, S. K. & Yamagata, T. Influence of the Indian Ocean Dipole on the Southern Oscillation. *J. Meteorol. Soc. Jpn.* **81**, 169–177 (2003).
16. Rodríguez-Fonseca, B. et al. Are Atlantic Niños enhancing Pacific ENSO events in recent decades? *Geophys. Res. Lett.* **36**, L20705 (2009).
17. Polo, I., Martin-Rey, M., Rodriguez-Fonseca, B., Kucharski, F. & Mechoso, C. R. Processes in the Pacific La Niña onset triggered by the Atlantic Niño. *Clim. Dyn.* **44**, 115–131 (2015).
18. Zhang, L., Wang, G., Newman, M. & Han, W. Interannual to decadal variability of tropical Indian Ocean sea surface temperature: Pacific influence versus local internal variability. *J. Clim.* **34**, 2669–2684 (2021).
19. Kido, S., Richter, I., Tozuka, T. & Chang, P. Understanding the interplay between ENSO and related tropical SST variability using linear inverse models. *Clim. Dyn.* **61**, 1029–1048 (2023).
20. Wang, J.-Z. & Wang, C. Joint boost to super El Niño from the Indian and Atlantic Oceans. *J. Clim.* **34**, 4937–4954 (2021).
21. Ham, Y.-G., Kug, J.-S., Park, J.-Y. & Jin, F.-F. Sea surface temperature in the north tropical Atlantic as a trigger for El Niño/Southern Oscillation events. *Nat. Geosci.* **6**, 112–116 (2013).
22. Wang, L., Yu, J. Y. & Paek, H. Enhanced biennial variability in the Pacific due to Atlantic capacitor effect. *Nat. Commun.* **8**, 14887 (2017).
23. Lübbecke, J. F. Tropical Atlantic warm events. *Nat. Geosci.* **6**, 22–23 (2013).
24. Richter, I. & Tokinaga, H. The Atlantic zonal mode: dynamics, thermodynamics, and teleconnections. In: *Tropical and extratropical air-sea interactions* (ed. Behera, S. K.) 171–206 (Elsevier, 2021). https://doi.org/10.1016/B978-0-12-818156-0.00008-3.
25. Lübbecke, J. F. et al. Equatorial Atlantic variability—modes, mechanisms, and global teleconnections. *WIREs Clim. Change* **9**, e527 (2018).
26. Ham, Y.-G., Kug, J.-S. & Park, J.-Y. Two distinct roles of Atlantic SSTs in ENSO variability: North Tropical Atlantic SST and Atlantic Niño. *Geophys. Res. Lett.* **40**, 4012–4017 (2013).
27. Hounsou-Gbo, A., Servain, J., Vasconcelos Junior, F. D. C., Martins, E. S. P. R. & Araújo, M. Summer and winter Atlantic Niño: connections with ENSO and implications. *Clim. Dyn.* **55**, 2939–2956 (2020).
28. Martín-Rey, M., Rodríguez-Fonseca, B., Polo, I. & Kucharski, F. On the Atlantic–Pacific Niños connection: a multidecadal modulated mode. *Clim. Dyn.* **43**, 3163–3178 (2014).
29. Park, J.-H. et al. Distinct decadal modulation of Atlantic-Niño influence on ENSO. *npj Clim. Atmos. Sci.* **6**, 105 (2023).
30. Losada, T. et al. Tropical response to the Atlantic Equatorial mode: AGCM multimodel approach. *Clim. Dyn.* **35**, 45–52 (2010).

31. Ding, H., Keenlyside, N. S. & Latif, M. Impact of the Equatorial Atlantic on the El Niño Southern Oscillation. *Clim. Dyn.* **38**, 1965–1972 (2012).
32. Kucharski, F. et al. The teleconnection of the tropical Atlantic to Indo-Pacific sea surface temperatures on inter-annual to centennial time scales: a review of recent findings. *Atmosphere* **7**, 29 (2016).
33. Jiang, L. & Li, T. Impacts of Tropical North Atlantic and Equatorial Atlantic SST anomalies on ENSO. *J. Clim.* **34**, 5635–5655 (2021).
34. Liu, S., Chang, P., Wan, X., Yeager, S. G. & Richter, I. Role of the Maritime Continent in the remote influence of Atlantic Niño on the Pacific. *Nat. Commun.* **14**, 3327 (2023).
35. McPhaden, M. J. The 2020–2022 triple-dip La Niña [in 'State of the Climate in 2022']. *Bull. Am. Meteorol. Soc.* **104**, S157–S158 (2023).
36. Hasan, N. A., Chikamoto, Y. & McPhaden, M. J. The influence of tropical basin interactions on the 2020–2022 double-dip La Niña. *Front. Clim.* **4**, 1001174 (2022).
37. Exarchou, E. et al. Impact of equatorial Atlantic variability on ENSO predictive skill. *Nat. Commun.* **12**, 1612 (2021).
38. Keenlyside, N. S., Ding, H. & Latif, M. Potential of equatorial Atlantic variability to enhance El Niño prediction. *Geophys. Res. Lett.* **40**, 2278–2283 (2013).
39. Frauen, C., Dommenget, D., Tyrrell, N., Rezny, M. & Wales, S. Analysis of the nonlinearity of El Niño–Southern oscillation teleconnections*. *J. Clim.* **27**, 6225–6244 (2014).
40. Martín-Rey, M., Rodríguez-Fonseca, B. & Polo, I. Atlantic opportunities for ENSO prediction. *Geophys. Res. Lett.* **42**, 6802–6810 (2015).
41. Dayan, H., Vialard, J., Izumo, T. & Lengaigne, M. Does sea surface temperature outside the tropical Pacific contribute to enhanced ENSO predictability? *Clim. Dyn.* **43**, 1311–1325 (2014).
42. Crespo-Miguel, R., Polo, I., Mechoso, C. R., Rodríguez-Fonseca, B. & Cao-García, F. J. ENSO coupling to the equatorial Atlantic: analysis with an extended improved recharge oscillator model. *Front. Mar. Sci.* **9**, 1001743 (2023).
43. Crespo, L. R., Belén Rodríguez-Fonseca, M., Polo, I., Keenlyside, N. & Dommenget, D. Multidecadal variability of ENSO in a recharge oscillator framework. *Environ. Res. Lett.* **17**, 074008 (2022).
44. Jiang, F. et al. Resolving the Tropical Pacific/Atlantic Interaction Conundrum. *Geophys. Res. Lett.* **50**, e2023GL103777 (2023).
45. Richter, I., Tokinaga, H., Kosaka, Y., Doi, T. & Kataoka, T. Revisiting the Tropical Atlantic influence on El Niño–Southern oscillation. *J. Clim.* **34**, 8533–8548 (2021).
46. Richter, I., Kosaka, Y., Kido, S. & Tokinaga, H. The tropical Atlantic as a negative feedback on ENSO. *Clim. Dyn.* **61**, 309–327 (2023).
47. Xie, S. P. et al. Global warming pattern formation: sea surface temperature and rainfall. *J. Clim.* **23**, 966–986 (2010).
48. Armstrong McKay, D. I. et al. Exceeding 1.5 °C global warming could trigger multiple climate tipping points. *Science* **377**, eabn7950 (2022).
49. Chou, C. & Neelin, J. D. Mechanisms of global warming impacts on regional tropical precipitation. *J. Clim.* **17**, 2688–2701 (2004).
50. DiNezio, P. N. et al. Climate response of the equatorial pacific to global warming. *J. Clim.* **22**, 4873–4892 (2009).
51. Held, I. M. & Soden, B. J. Robust responses of the hydrological cycle to global warming. *J. Clim.* **19**, 5686–5699 (2006).
52. Huang, P., Xie, S. P., Hu, K., Huang, G. & Huang, R. Patterns of the seasonal response of tropical rainfall to global warming. *Nat. Geosci.* **6**, 357–361 (2013).
53. Cai, W. et al. Increased frequency of extreme La Niña events under greenhouse warming. *Nat. Clim. Change* **5**, 132–137 (2015).
54. Cai, W. et al. Increased variability of eastern Pacific El Niño under greenhouse warming. *Nature* **564**, 201–206 (2018).
55. Yang, Y. et al. Suppressed Atlantic Niño/Niña variability under greenhouse warming. *Nat. Clim. Change* **12**, 814–821 (2022).
56. Crespo, L. R. et al. Weakening of the Atlantic Niño variability under global warming. *Nat. Clim. Change* **12**, 822–827 (2022).
57. Prigent, A., Lübbecke, J. F., Bayr, T., Latif, M. & Wengel, C. Weakened SST variability in the tropical Atlantic Ocean since 2000. *Clim. Dyn.* **54**, 2731–2744 (2020).
58. Tokinaga, H. & Xie, S.-P. Weakening of the equatorial Atlantic cold tongue over the past six decades. *Nat. Geosci.* **4**, 222–226 (2011).
59. Prigent, A., Imbol Koungue, R. A., Imbol Nkwinkwa, A. S. N., Beobide-Arsuaga, G. & Farneti, R. Uncertainty on Atlantic Niño variability projections. *Geophys. Res. Lett.* **50**, e2023GL105000 (2023).
60. Jia, F. et al. Weakening Atlantic Niño–Pacific connection under greenhouse warming. *Sci. Adv.* **5**, eaax4111 (2019).
61. Knutson, T. R. & Manabe, S. Time-mean response over the tropical Pacific to increased CO_2 in a coupled ocean-atmosphere model. *J. Clim.* **8**, 2181–2199 (1995).
62. Ma, J., Xie, S. P. & Kosaka, Y. Mechanisms for tropical tropospheric circulation change in response to global warming. *J. Clim.* **25**, 2979–2994 (2012).
63. Wang, R., He, J., Luo, J. & Chen, L. Atlantic warming enhances the influence of Atlantic Niño on ENSO. *Geophys. Res. Lett.* **51**, e2023GL108013 (2024).
64. Capotondi, A. et al. Understanding ENSO diversity. *Bull. Am. Meteorol. Soc.* **96**, 921–938 (2015).
65. Zhang, L. et al. Emergence of the Central Atlantic Niño. *Sci. Adv*. **9**, eadi5507 (2023).
66. Gadgil, S., Joseph, P. V. & Joshi, N. V. Ocean–atmosphere coupling over monsoon regions. *Nature* **312**, 141–143 (1984).
67. Graham, N. E. & Barnett, T. P. Sea surface temperature, surface wind divergence, and convection over tropical oceans. *Science* **238**, 657–659 (1987).
68. Waliser, D. E., Lau, K. M. & Kim, J.-H. The influence of coupled sea surface temperatures on the Madden–Julian oscillation: a model perturbation experiment. *J. Atmos. Sci.* **56**, 333–358 (1999).
69. Chen, B., Zhang, L. & Wang, C. Distinct impacts of the Central and Eastern Atlantic Niño on the European climate. *Geophys. Res. Lett.* **51**, e2023GL107012 (2024).
70. Martín-Rey, M., Polo, I., Rodríguez-Fonseca, B. & Kucharski, F. Changes in the interannual variability of the tropical Pacific as a response to an equatorial Atlantic forcing. *Sci. Mar.* **76**, 105–116 (2012).
71. Martín-Rey, M., Polo, I., Rodríguez-Fonseca, B., Losada, T. & Lazar, A. Is there evidence of changes in tropical Atlantic variability modes under AMO phases in the observational record? *J. Clim.* **31**, 515–536 (2018).
72. Martín-Rey, M., Polo, I., Rodríguez-Fonseca, B., Lazar, A. & Losada, T. Ocean dynamics shapes the structure and timing of Atlantic equatorial modes. *J. Geophys. Res. Oceans* **124**, 7529–7544 (2019).
73. Losada, T. & Rodríguez-Fonseca, B. Tropical atmospheric response to decadal changes in the Atlantic Equatorial Mode. *Clim. Dyn.* **47**, 1211–1224 (2016).
74. Losada, T., Rodríguez-Fonseca, B. & Kucharski, F. Tropical influence on the summer Mediterranean climate. *Atmos. Sci. Lett.* **13**, 36–42 (2012).
75. Silva, P., Wainer, I. & Khodri, M. Changes in the equatorial mode of the Tropical Atlantic in terms of the Bjerknes Feedback Index. *Clim. Dyn.* **56**, 3005–3024 (2021).
76. Richter, I. et al. Multiple causes of interannual sea surface temperature variability in the equatorial Atlantic Ocean. *Nat. Geosci.* **6**, 43–47 (2013).
77. Zhang, L. & Han, W. Indian Ocean dipole leads to Atlantic Niño. *Nat. Commun.* **12**, 5952 (2021).
78. Wang, C., Zhang, L., Lee, S.-K., Wu, L. & Mechoso, C. R. A global perspective on CMIP5 climate model biases. *Nat. Clim. Change* **4**, 201–205 (2014).
79. Yang, Y., Cheng, X., Wu, L., Cai, W. & Chen, Y. Mechanisms of model bias impacting responses of the Atlantic cold tongue to greenhouse warming. *Environ. Res. Lett.* **19**, 024037 (2024).

80. Schneider, T., Bischoff, T. & Haug, G. H. Migrations and dynamics of the intertropical convergence zone. *Nature* **513**, 45–53 (2014).
81. Watanabe, M., Jin, F.-F. & Kimoto, M. Tropical axisymmetric mode of variability in the atmospheric circulation: dynamics as a neutral mode*. *J. Clim.* **15**, 1537–1554 (2002).
82. Chiang, J. C. H. & Friedman, A. R. Extratropical cooling, interhemispheric thermal gradients, and tropical climate change. *Annu. Rev. Earth Planet. Sci.* **40**, 383–412 (2012).
83. Lee, J.-Y. & Wang, B. Future change of global monsoon in the CMIP5. *Clim. Dyn.* **42**, 101–119 (2014).
84. Wang, B., Liu, J., Kim, H.-J., Webster, P. J. & Yim, S.-Y. Recent change of the global monsoon precipitation (1979–2008). *Clim. Dyn.* **39**, 1123–1135 (2012).
85. Timmermann, A. et al. The influence of a weakening of the Atlantic meridional overturning circulation on ENSO. *J. Clim.* **20**, 4899–4919 (2007).
86. Dong, B. & Sutton, R. T. Enhancement of ENSO variability by a weakened Atlantic thermohaline circulation in a coupled GCM. *J. Clim.* **20**, 4920–4939 (2007).
87. Zhang, R. & Delworth, T. L. Simulated tropical response to a substantial weakening of the Atlantic thermohaline circulation. *J. Clim.* **18**, 1853–1860 (2005).
88. Sigmond, M., Fyfe, J. C., Saenko, O. A. & Swart, N. C. Ongoing AMOC and related sea-level and temperature changes after achieving the Paris targets. *Nat. Clim. Change* **10**, 672–677 (2020).
89. Xie, S.-P. On the genesis of the equatorial annual cycle. *J. Clim.* **7**, 2008–2013 (1994).
90. Sobel, A. H., Nilsson, J. & Polvani, L. M. The weak temperature gradient approximation and balanced tropical moisture waves*. *J. Atmos. Sci.* **58**, 3650–3665 (2001).
91. Johnson, N. C. & Xie, S.-P. Changes in the sea surface temperature threshold for tropical convection. *Nat. Geosci.* **3**, 842–845 (2010).
92. Zhang, W., Jiang, F., Stuecker, M. F., Jin, F.-F. & Timmermann, A. Spurious North Tropical Atlantic precursors to El Niño. *Nat. Commun.* **12**, 3096 (2021).
93. Rayner, N. A. et al. Global analyses of sea surface temperature, sea ice, and night marine air temperature since the late nineteenth century. *J. Geophys. Res.* **108**, 4407 (2003).
94. Deser, C., Phillips, A. S. & Alexander, M. A. Twentieth century tropical sea surface temperature trends revisited. *Geophys. Res. Lett.* **37**, L10701 (2010).
95. Riahi, K. et al. The Shared Socioeconomic Pathways and their energy, land use, and greenhouse gas emissions implications: an overview. *Glob. Environ. Chang.* **42**, 153–168 (2017).
96. Neale, R. B. et al. Description of the NCAR Community Atmosphere Model (CAM 5.0). https://doi.org/10.5065/wgtk-4g06 (2012).

Acknowledgements

We acknowledge the modeling groups, the Program for Climate Model Diagnosis and Intercomparison (PCMDI), and the World Climate Research Programme (WCRP) for their roles in making available CMIP6 datasets. C.W. is supported by the National Natural Science Foundation of China grant W2441014, 42192564, the National Key R&D Program of China grant 2019YFA0606701, the Strategic Priority Research Program of the Chinese Academy of Sciences grant XDB42000000, and the development fund of South China Sea Institute of Oceanology of the Chinese Academy of Sciences grant SCSIO202208. L.Z. is supported by Development fund (SCSIO202203) and Special fund (SCSIO2023QY01) of South China Sea Institute of Oceanology of the Chinese Academy of Sciences, and the GuangDong Basic and Applied Basic Research Foundation (2024B1515040024). W.X. is supported by the National Natural Science Foundation of China (42306030) and National Key R&D Program of China: Young Scientist Program (2023YFC3108800). A.H. is supported by the Regional and Global Model Analysis (RGMA) component of the Earth and Environmental System Modeling Program of the U.S. Department of Energy's Office of Biological & Environmental Research (BER) via National Science Foundation (NSF) IA 1947282 (DE-SC0022070). The National Center for Atmospheric Research is sponsored by the NSF of the United States of America under Cooperative Agreement No. 1852977. This is PMEL Contribution No. 5592.

Author contributions

L.Z. conceived the study and wrote the initial manuscript in discussion with C.W. L.Z. conducted the analysis and prepared the figures. B.C. conducted the atmospheric model experiments. H.L. performed the LBM experiments. All the authors contributed to interpretating results and improving the paper.

Competing interests

The authors declare no competing interests.

Additional information

Supplementary information The online version contains supplementary material available at https://doi.org/10.1038/s41612-025-01105-w.

Correspondence and requests for materials should be addressed to Lei Zhang or Chunzai Wang.